ACS APPLIED MATERIALS & INTERFACES

Research Article

www.acsami.org

A Facile Surfactant-Assisted Reflux Method for the Synthesis of Single-Crystalline Sb_2Te_3 Nanostructures with Enhanced Thermoelectric Performance

Heng Quan Yang,[†,‡] Lei Miao,[*,†,⊥] Cheng Yan Liu,[†] Chao Li,[§] Sawao Honda,[∥] Yuji Iwamoto,[∥] Rong Huang,[§] and Sakae Tanemura[†]

[†]Key Laboratory of Renewable Energy, Guangzhou Institute of Energy Conversion, Chinese Academy of Sciences, Guangzhou 510640, P. R. China

[‡]University of Chinese Academy of Sciences, Beijing 100049, P. R. China

[§]Key Laboratory of Polarized Materials and Devices, Ministry of Education, East China Normal University, Shanghai 200062, P. R. China

[∥]Department of Frontier Materials, Graduate School of Engineering, Nagoya Institute of Technology, Gokiso-cho, Showa-ku, Nagoya 466-8555, Japan

[⊥]School of Material Science and Engineering, Guilin University of Electronic Technology, Guilin 51004, P. R. China

Supporting Information

ABSTRACT: Antimony telluride (Sb_2Te_3) and its based alloys are of importance to p-type semiconductors for thermoelectric applications near room temperature. Herein, we report a simple, low-energy intensive, and scalable surfactant-assisted reflux method for the synthesis of Sb_2Te_3 nanoparticles in the solvent ethylene glycol (EG) at low temperatures (120−180 °C). The formation mechanism of platelike Sb_2Te_3 nanoparticles is proposed. Also, it is found that the size, shape, and chemical composition of the products could be controlled by the introduction of organic surfactants (CTAB, PVP, etc.) or inorganic salts (EDTA-Na_2, NaOH, etc.). Additionally, the collected Sb_2Te_3 nanoparticles were further fabricated into nanostructured pellets using cold-compaction and annealing techniques. Low resistivity [(7.37−19.4) × 10^{-6} Ω m], moderate Seebeck coefficient (103−141 μV K^{-1}), and high power factor (10−16 × 10^{-4} W m^{-1} K^{-2}) have been achieved in our Sb_2Te_3-nanostructured bulk materials. The relatively low thermal conductivity (1.32−1.55 W m^{-1} K^{-1}) is attained in the nanobulk made of PVP-modified nanoparticles, and values of ZT in the range of 0.24−0.37 are realized at temperatures ranging from 50 to 200 °C. Our researches set forth a new avenue in promoting practical applications of Sb_2Te_3-based thermoelectric power generation or cooling devices.

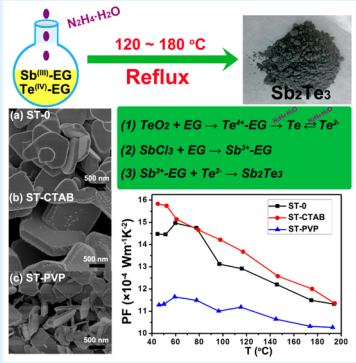

KEYWORDS: *antimony telluride, growth mechanism, reflux method, thermoelectric materials, transport properties*

1. INTRODUCTION

Thermoelectric effects realize the inverse transformation between heat and electricity with the help of the directional drift of electrons or holes from the hot side to the cold one in the solid-state conductors.[1−3] The conversion efficiency of thermoelectric materials is related to the dimensionless figure of merit $ZT = S^2T/\rho\kappa$, where T, S, ρ, and κ are the absolute temperature, Seebeck coefficient, resistivity, and thermal conductivity, respectively.[1−7] Unfortunately, the wide and extensive practical applications of thermoelectric materials are limited by their low ZT values. However, recent studies show that the ZT value of telluride-based thermoelectric materials can be remarkably improved through suppression of the lattice conductivity by the engineered point defects and grain boundaries to strengthen the phonon scattering.[8−12]

Antimony telluride (Sb_2Te_3) and its based alloys are the well-known p-type thermoelectric materials for near room temperature applications because of their narrow band gaps, their indirect multivalley band structures, and the existence of heavy elements.[7,13,14] However, the thermodynamic self-generation of antisite defects, Sb_{Te}', creates a large number of holes in the bulk, generally resulting in low Seebeck coefficients and ZT values.[15−18] In addition to restricting these kinds of antisite defects or reducing the hole concentration in the Sb_2Te_3 matrix by the incorporation of appropriate elements (bismuth,[9,10] sulfide,[19] indium,[20,21] etc.), grain boundary engineering is also an indispensable approach for low-energy carrier filtering.

As mentioned above, microstructures and nanostructures are generally applied in thermoelectric materials with the purposes of enhancing the phonon scattering and reinforcing the low-energy carrier filtering by the designed boundaries. Therefore, it is necessary to explore simple and low-cost synthetic approaches to

Received: March 22, 2015
Accepted: June 10, 2015
Published: June 10, 2015

DOI: 10.1021/acsami.5b02504
ACS Appl. Mater. Interfaces 2015, 7, 14263−14271

synthesize nano/microparticles with controlled and regulated chemical composition, shape, and size. Many chemical strategies, involving a microwave-assisted solvothermal route,[22−25] a hydro/solvothermal method,[26−37] a heating reflux method,[38−40] electrochemical deposition,[41−43] thermal decomposition[44−46] and others,[47−50] have been employed for the synthesis of Sb_2Te_3 nanoparticles. However, many of these methods are not suitable for the preparation of Sb_2Te_3 nanoparticles on a large scale owing to the high cost or bad reproducibility. Also, the pure phase of Sb_2Te_3 nanostructures has not been easily attained so far because of the spontaneous occupation of partial Sb atoms at Te lattice sites and the effortless separation of the Te element from the Sb_2Te_3 matrix.[15] The existence of a large amount of Te may remarkably reduce the electrical conductivity of the Sb_2Te_3 matrix, resulting in the degradation of *ZT*. On the contrary, a small amount of Te uniformly located in the Sb_2Te_3 matrix can probably act as a low-energy carrier and phonon scattering center, facilitating enhancement of the Seebeck coefficient and depression of the thermal conductivity without doing much harm to the electrical conductivity.

Here we report a simple and low-energy consumption reflux method for the synthesis of Sb_2Te_3 nanostructures in the solvent EG at low temperatures (120−180 °C), with which it is much easier to obtain Sb_2Te_3 powder on a large scale. Because of the advantages of the reflux method such as low cost, easy manipulation, and better contact of the reactants, it is a very convenient to extend this method for the commercial fabrication of nanoparticles with well-defined size, shape, and chemical composition. As an alternative, thanks to the strong dissolving capability of low polyhydric alcohol with regard to some metal salts (chlorides or nitrates) and oxides as well as the reasonable evolution mechanism of Sb_2Te_3 nanoplates that we proposed, we have successfully synthesized a crop of chalcogenides (M−X, where M = Sb, Bi, Pb, Sn, etc., and X = Te, Se, S) with good crystallization by employing this excellent reflux method. Synthesizing these chalcogenides under the same condition may be beneficial to obtaining the doped or alloyed targets through a one-pot reaction, extending the routes to achieve the multicomponent thermoelectric materials. Furthermore, the organic surfactants (CTAB, PVP, etc.) and inorganic salts (EDTA-Na_2, NaOH, etc.) were introduced for modulation of the size, shape, and chemical composition of the resultant products, which has not yet received much concern in the EG reaction system. In addition, low electrical resistivity and moderate Seebeck coefficient have been achieved in our Sb_2Te_3-nanostructured bulk materials. The PVP residues decorated on the surface of Sb_2Te_3 nanoparticles can effectively strengthen the phonon scattering and enhance the low-energy carrier filtering by the boundaries, leading to the remarkable decrease of the thermal conductivity and the evident increase of the Seebeck coefficient, respectively. As a result, the nanobulk made of the PVP-decorated Sb_2Te_3 nanoparticles achieves the highest *ZT* of 0.37 at 200 °C, having a potential for thermoelectric applications. Our surfactant-assisted reflux method enables effective tailoring of the morphology, size, and chemical composition of the resultant Sb_2Te_3 nanoparticles, which opens a new horizon of controlling the property of the relevant devices. Hence, our work shortens the distance of Sb_2Te_3-based thermoelectric applications toward low-temperature power generation and system cooling for improved energy conservation.

2. EXPERIMENTAL SECTION

2.1. Chemical Reagents. Antimony trichloride ($SbCl_3$), tellurium dioxide (TeO_2), ethylene glycol (EG), hydrazine hydrate ($N_2H_4{\cdot}H_2O$, 98%), cetyltrimethylammonium bromide (CTAB), poly-(vinylpyrrolidone) (PVP; K-30), ethylenediaminetetraacetic acid disodium salt (EDTA-Na_2), and sodium hydroxide (NaOH) were purchased from Aladdin Industrial Corp., Shanghai, China. All of the chemicals were analytical grade and were used without further purification.

2.2. Synthesis of Sb_2Te_3 Nanostructures. In a typical synthesis process, 1.3950 g (6.12 mmol) of $SbCl_3$ was dissolved into 50 mL of EG, which formed a clear and transparent solution by heating at 50 °C and stirring. Then the as-prepared $SbCl_3$ solution was poured into a one-neck round-bottom flask, containing 1.4364 g (9 mmol) of TeO_2 and a given amount of organic surfactants or inorganic salts (such as CTAB, PVP, EDTA-Na_2, NaOH, etc.). Similarly, a transparent solution was also formed after another 100 mL of EG was added into the flask, which was put on a heating mantle and heated at 150−180 °C. Then 4 mL of $N_2H_4{\cdot}H_2O$ was added to the obtained transparent solution after cooling to ∼120 °C, and the solution quickly became dark in a few seconds. (***Attention!*** *It is too dangerous to add $N_2H_4{\cdot}H_2O$ at higher temperatures, ≥150 °C, because a large amount of gas (or foam) can be generated as soon as hydrazine is added.*) Finally, the solution was maintained at 120−180 °C for 24 h and cooled to room temperature naturally. The gray precipitates were collected after washing using absolute ethanol and drying under vacuum at 80 °C for 6 h.

2.3. Fabrication of Sb_2Te_3 Nanobulk Materials. Sb_2Te_3 nanobulk pellets (3 mm × 15 mm × 15 mm) were fabricated from the collected gray powder via cold compaction (∼1000 MPa) and annealing under mixed gas (8% H_2 + 92% Ar) protection at 350 °C for 12 h (∼80%, relative density). The flow rate of protective gases was 0.15 L min^{-1}, and the heating rate of the tubular furnace was 5 °C min^{-1}. Prisms of 2.5 mm × 3 mm × 15 mm were cut from the as-annealed pellets for electrical resistivity and Seebeck coefficient measurements, and the rest of the pellets were polished into cuboids with sizes of ∼2 mm × 12 mm × 15 mm for thermal diffusivity measurement; other batches of Sb_2Te_3 nanopellets were fabricated under the same conditions and processed into thin pellets with sizes of ∼0.6 mm × 10 mm × 10 mm for the Hall measurements.

2.4. Characterization. The crystal structures of the powders were examined by powder diffractometry (PANalytical X'pert Pro MPD operated at 40 kV and 40 mA, Cu Kα, λ = 0.154 nm). Their morphology was observed by field-emission scanning electron microscopy (SEM; Hitachi S-4800, Japan) and field-emission transmission electron microscopy (TEM; JEOL-2100F, Japan). The crystal structure and composition were examined by selected area electron diffraction (SAED) and energy-dispersive spectroscopy (EDS; Genesis 2000, Edax Instrument, USA), respectively. The Fourier transform infrared (FTIR) spectra of the collected Sb_2Te_3 samples were measured using a KBr tablet method by a FTIR spectrometer (TENSOR 27, Bruker, Germany) at room temperature. The electrical resistivity (ρ) and Seebeck coefficient (S) were measured by the static direct-current (dc) method (ZEM-3, ULVAC RIKO, Japan) in a low-helium (99.999%) atmosphere with a temperature gradient from 20 to 40 °C in a step of 10 °C. The carrier mobility and concentration were determined using a dc Hall measurement system at excitation currents of up to 100 mA and magnetic fields of up to 1.5 T (model 8404, Lake Shore Cryotronics, USA). The thermal conductivity (κ) is calculated from $\kappa = D\rho' C_p$, where D is the thermal diffusivity, C_p is the specific heat, and ρ' is the volume density. The thermal diffusivity (D) was measured by a laser flash method (TC-7000, ULVAC RIKO, Japan), the specific heat was determined by differential scanning calorimetry (DSC; DSC-8270, Rigaku, Japan), and the volume density (ρ') was calculated from the mass and volume of the Sb_2Te_3 pellets.

3. RESULTS AND DISCUSSION

3.1. Structure, Morphology, and Reaction Mechanism. Figure 1 shows the typical X-ray diffraction (XRD) pattern of the Sb_2Te_3 powder prepared via a heating reflux method in the

DOI: 10.1021/acsami.5b02504
ACS Appl. Mater. Interfaces 2015, 7, 14263−14271

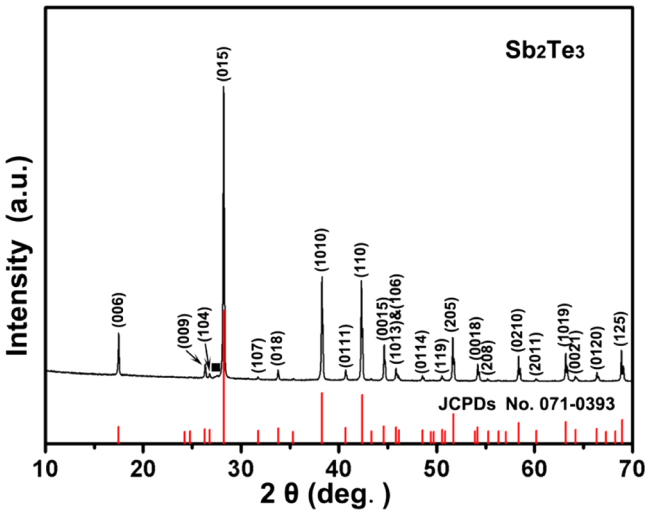

Figure 1. XRD pattern of Sb_2Te_3 nanoparticles synthesized at 120 °C for 24 h. The black square (■) stands for Te.

solvent EG at 120 °C for 24 h, which can be readily indexed to the rhombohedral phase of Sb_2Te_3 (JCPD No. 071-0393). The sharp diffraction peaks indicate that our samples have a good crystallinity. Just an extremely weak diffraction peak at 27.55° is indexed to Te (JCPD No. 004-0555). The composition of our Sb_2Te_3 powder has been confirmed by EDS analysis. The atomic ratio between Sb and Te is around 41:59, which is close to the stoichiometric ratio of Sb_2Te_3. This conflicting result of EDS and XRD detection can be attributed to the spontaneously formed antisite defects of Sb_{Te}'.

SEM and TEM have been used to characterize the morphology and structure of our Sb_2Te_3 nanoparticles. Low-resolution SEM images (Figure 2a,b) show that the irregular Sb_2Te_3 nanoplates have a wide size distribution. It is estimated that the plane size of Sb_2Te_3 nanoplates is in the range of 1−3 μm and the thickness is from 100 to 350 nm. High-resolution TEM (HRTEM) studies (Figure 2c) corroborate that the Sb_2Te_3 sheets have a preferential growth direction perpendicular to the *c* axis, which originated

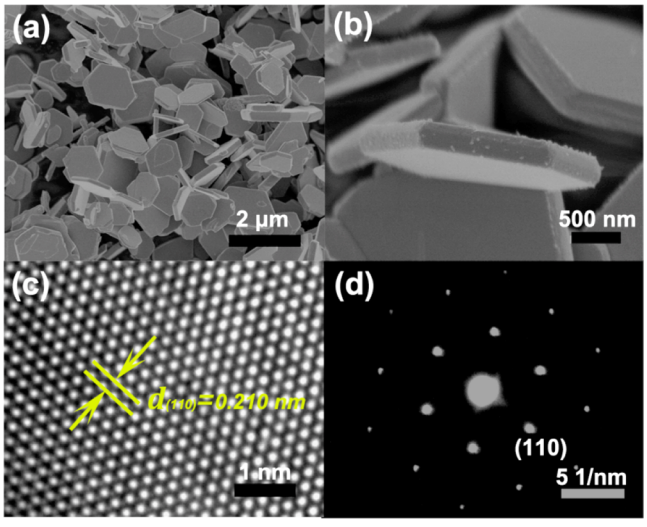

Figure 2. Morphology and structure of Sb_2Te_3 nanoparticles synthesized at 120 °C for 24 h: (a) low-magnification SEM image; (b) high-magnification SEM image; (c) HRTEM image; (d) SAED pattern taken from an individual Sb_2Te_3 nanoplate.

from the highly anisotropic crystal structure of Sb_2Te_3. The SAED pattern collected on a single Sb_2Te_3 nanoplate is shown in Figure 2d. The spot pattern clearly shows the single crystalline nature of our Sb_2Te_3 nanoplates, which is consistent with the result of HRTEM.

To demonstrate the formation mechanism of the Sb_2Te_3 nanosheets, systematic time-dependent experiments were carried out. The phase structure and morphology of the samples prepared at 120 °C for different reaction times (30 min and 6 and 12 h) were characterized by XRD and SEM, respectively. As illustrated in Figure 3a,b, nanowires with diameters of 100−200

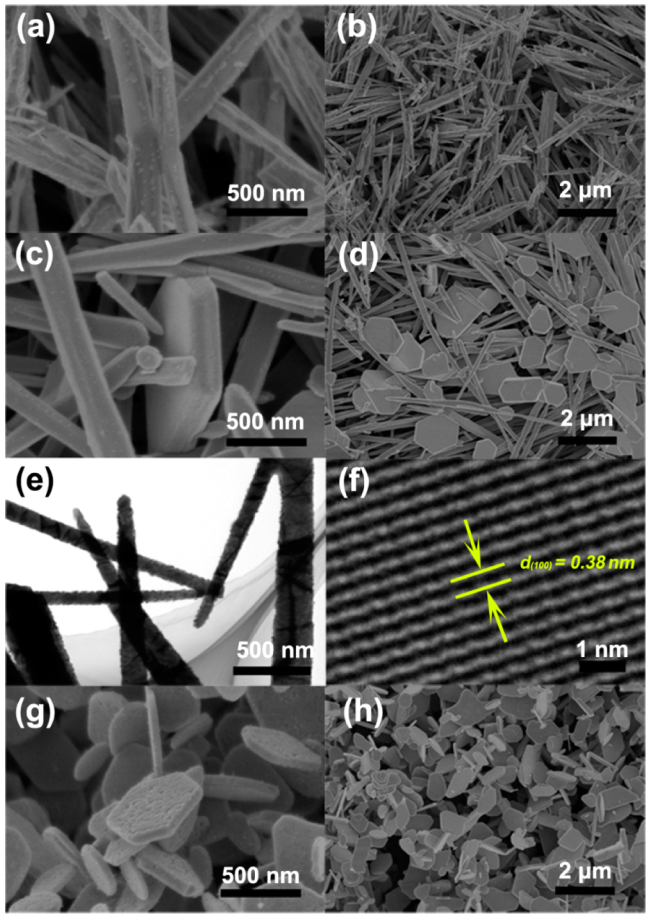

Figure 3. SEM, TEM, and HRTEM images of the products synthesized at 120 °C for different reaction times: (a and b) 30 min; (c−f) 6 h; (g and h) 12 h. Notably, parts e and f are the TEM and HRTEM images taken on the Te nanostructures intentionally.

nm and lengths of 2−5 μm are formed at the first step. The XRD result shows that it is the element of Te with a hexagonal structure (JCPD No. 004-0555), as shown in Figure 4a. Obviously, Te^{4+}-EG is easily reduced by hydrazine, resulting in the formation of Te. Also, Te in one-dimensional morphology can be attributed to its anisotropic crystal structure, which prefers to grow along with the [001] direction. As the reaction proceeds for 6 h, Te nanowires are likely to grow into nanoribbons and become much longer (>10 μm) but without obviously changing in diameter, as illustrated in Figure 3c,d. Also, their morphology and structure are further characterized by TEM, as displayed in Figure 3e,f. The lattice fringes with a spacing of 0.38 nm confirm that these one-dimensional nanoparticles are the Te element. At the same time, a certain number of irregular hexagonal Sb_2Te_3

DOI: 10.1021/acsami.5b02504
ACS Appl. Mater. Interfaces 2015, 7, 14263−14271

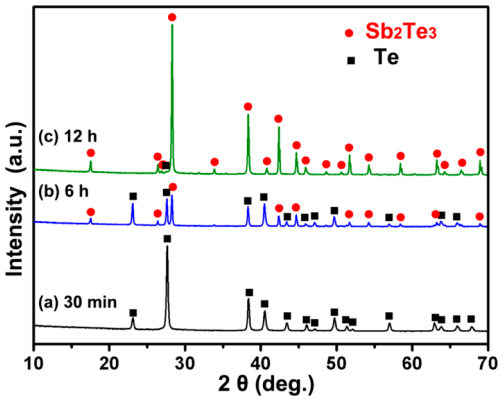

Figure 4. XRD patterns of the products synthesized at 120 °C for different times: (a) 30 min; (b) 6 h; (c) 12 h.

nanoplates generate, which has been confirmed by XRD detection, as indicated in Figure 4b. As the reaction time increases to 12 h, the product is dominated by the irregular nanoplates, with the plane size ranging from 500 nm to 2 μm and a thickness of about 50 nm, as seen in Figure 3g,h. All of the peaks of the XRD pattern are indexed to Sb_2Te_3 in the rhombohedral structure (Figure 4c) except a weak peak at 27.55° belongs to Te. As the reaction goes a step further, the Ostwald ripening process will undergo.[51,52] As a result, both the thickness and plane size of the Sb_2Te_3 nanoplates will increase, as shown in Figure 2a,b.

On the basis of the above experimental results, we can readily propose the whole morphology evolution process of the Sb_2Te_3 nanosheets. $SbCl_3$ and TeO_2 are initially dissolved by EG and form complex ions of Sb^{3+}-EG and Te^{4+}-EG at 150−180 °C, respectively. Element Te is generated immediately once hydrazine is added into the above solution. According to the previous reports, it could be generally accepted that the disproportionation reaction of Te ($3Te + 6OH^- \rightleftharpoons TeO_3^{2-} + 2Te^{2-} + 3H_2O$) only takes place in strong alkaline solutions (pH $\gtrsim$ 13.8).[22,23,28,30,34,40] Judging from the low pH (8−9) value of our weak alkaline reaction system, it is hard for the disproportionation of Te to occur in this situation. Furthermore, the characteristic pink color of Te^{2-} will appear as Te is added into hydrazine hydrate directly. Thus, Te can be reduced to Te^{2-} by the hydrazine.[23] On the other hand, no element of Sb was obtained by mixing $SbCl_3$ or its EG solution with hydrazine hydrate, suggesting that it is difficult to reduce Sb^{3+} to element Sb by hydrazine in the EG system. Hence, the as-generated Te might be further reduced to Te^{2-} ions and react with Sb^{3+}-EG for the formation of Sb_2Te_3 nanoparticles until most of the element Te disappears. Thereby the reaction mechanism could be formulated as

$$TeO_2 + EG \rightarrow Te^{4+}\text{-}EG \xrightarrow{\text{hydrazine}} Te \underset{\Delta}{\overset{\text{hydrazine}}{\rightleftharpoons}} Te^{2-} \quad (1)$$

$$SbCl_3 + EG \rightarrow Sb^{3+}\text{-}EG \quad (2)$$

$$Sb^{3+}\text{-}EG + Te^{2-} \rightarrow Sb_2Te_3 \quad (3)$$

From the previous reports concerned with the growth mechanism of Bi_2Te_3 nanoparticles, the morphology of the nanowire and nanoplate can be obtained by employing the element diffusion and ion reaction mechanism, respectively.[53,54] For example, the synthesis of Bi_2Te_3 in nanowire morphology involved two steps in which nanowires of Te were first prepared and then the element of Bi diffused into the Te nanowire templates to form the compound nanowires. A similar diffusion reaction mechanism can be also found in the synthesis of nanowires of PbTe,[55,56] Ag_2Te,[57] etc. Except for the proper reaction temperature and time, we believe that there also exist two critical factors for the successful synthesis of these compound nanowires. One is that the metal colloids must be easily formed at the template surfaces by reduction of the corresponding metal ions. The other is that they keep the Te nanowires relatively stable. Bi_2Te_3 nanoplates could be obtained via the direct ion reaction between the thiolate-protected Bi^{3+} and the tri-*n*-octylphosphine-coordinated Te^{2-} in oleylamine.[54] Obviously, the two-dimensional morphology of the final Bi_2Te_3 product is determined by its intrinsic rhombohedral crystal structure.

However, the platelike morphology of the Sb_2Te_3 nanoparticle is mainly determined by its own crystal structure. As mentioned above, it is difficult for hydrazine to reduce the Sb^{3+} ions to the element Sb in a polyhydric alcohol reaction system. In addition to the low standard redox potential of the Sb^{3+}/Sb pair ($E^{\theta}_{Sb^{3+}/Sb}$ = −0.66 eV, alkaline), the role of hydroxyl in chelating with Sb^{3+} leads to a further decrease of the redox potential of the Sb^{3+}/Sb pair. In our case, EG molecules act as ligands and keep Sb^{3+} from being reduced. As a result, growth of the Sb_2Te_3 nanoparticle is dominated by the ion reaction mechanism. Also, the platelike morphology is determined by the layered crystal structure of Sb_2Te_3, which is composed of periodic stacking sheets of covalent bonding layers ($Te^{(1)}-Sb-Te^{(2)}-Sb-Te^{(1)}$) with weak van der Waals interaction in $Te^{(1)}-Te^{(1)}$. This unique layered structure results in preferential growth parallel to the *ab* plane of Sb_2Te_3 nanocrystals. Therefore, platelike Sb_2Te_3 nanoparticles will be formed naturally in our EG reaction system.

3.2. Effect of Organic Surfactants and Inorganics. The synthesis of nanomaterials with well-defined size, shape, and chemical composition appears to be one of the most popular research subjects over the past 2 decades.[58−60] Also, introducing the complexing agents into the reaction system is an effective way to control the growth rate and exposed crystallographic planes of the nanoparticles, leading to a specific morphology of the target nanomaterials.[58] In this section, we will investigate the effect of the organic surfactants (CTAB, PVP, etc.) and inorganic salts (EDTA-Na_2, NaOH, etc.) on the size, shape, and composition of the resultant Sb_2Te_3 nanoparticles. It is worth noting that some capping agents, such as PVP, can adhere strongly to the surface of the subtle particles and slow down the reaction rate rapidly, usually resulting in a certain amount of Te residues in the Sb_2Te_3 products at low reaction temperatures, i.e., 120 °C. Thus, a batch of experiments was carried out at a higher temperature of 180 °C to ensure the purity and reproducibility of our Sb_2Te_3 products with or without surfactants. The XRD detection results (Figure 5) confirm that all of the products are dominated by rhombohedral Sb_2Te_3.

Parts a and b of Figure 6 show irregular Sb_2Te_3 nanoplates with lengths of 700 nm to 3 μm and thicknesses of 50−150 nm synthesized at 180 °C without capping agents. In comparison with the products synthesized at 120 °C, the Sb_2Te_3 nanoplates obtained at 180 °C have a similar range in length and are nearly half decreased in thickness because of the ease with which the surface atoms escape from the lateral planes of the nanoplates during the Ostwald ripening process. Additionally, it is found that the verge of each plate is not sharp-cut and the number of plate edges is also decreased, demonstrating that the nanoparticle with sharp edges is inclined to transform into the one with a sphere surface at high temperatures. As a result, the particle becomes

DOI: 10.1021/acsami.5b02504
ACS Appl. Mater. Interfaces 2015, 7, 14263−14271

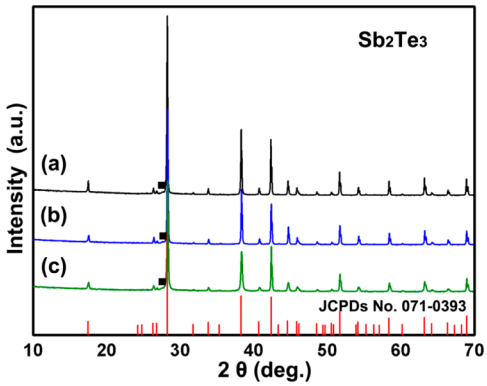

Figure 5. XRD patterns of Sb_2Te_3 nanoparticles synthesized at 180 °C for 24 h without or with surfactants: (a) without surfactant; (b) CTAB; (c) PVP. The black square (■) stands for Te.

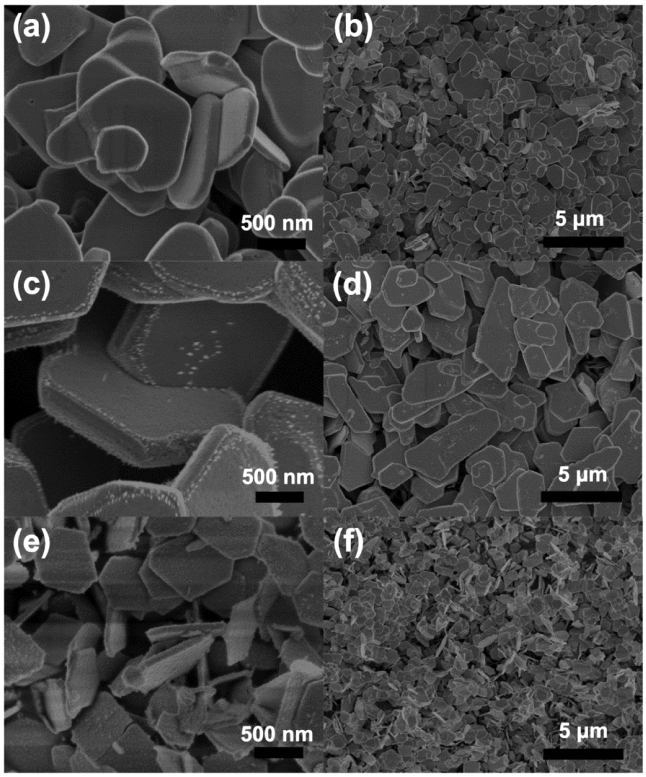

Figure 6. SEM images of Sb_2Te_3 nanoparticles synthesized at 180 °C for 24 h without or with surfactants: (a and b) without surfactant; (c and d) CTAB; (e and f) PVP.

thermodynamically stable because of the reduced surface Gibbs energy. However, with the addition of a long chain of capping agent (CTAB, 8.0 g), a mass of elongated Sb_2Te_3 nanoplates with lengths of 3−7 μm, widths of 1−2.5 μm, and thicknesses of 150−350 nm were formed (Figure 6c,d). To be different, the prominently anisotropic growth of Sb_2Te_3 nanoplates occurred in the presence of PVP (0.6 g). PVP is a polymeric capping agent and has a strong binding affinity with the nanoparticle surface, effectively hindering the atoms from continuously aggregating onto the lateral plane of the Sb_2Te_3 nanoplate. Therefore, the thickness of the nanoplate is below 100 nm and the decreased lateral length is in the range of 500 nm to 1.5 μm (Figure 6e,f). Additionally, it is a hard work to remove the organics from the surface of nanoparticles via washing. The FTIR spectra show that the surface of these collected Sb_2Te_3 nanoparticles is contaminated by the newly generated organics, which may come from the reaction of EG, $N_2H_4{\cdot}H_2O$, and Cl^-. Also, there still exist some PVP residues or derivatives on the surface of the corresponding collected Sb_2Te_3 nanoparticles (Figure S1 in the SI). However, only the PVP residues decorated on the surface of the Sb_2Te_3 nanoparticles could significantly modify their electrical and thermal transport properties; the details will be given in the next section.

As an alternative, it is found that the composition of the products can be conveniently tuned by alteration of the inorganics content, such as NaOH, EDTA-Na_2, etc. (Figure S2 in the SI). For example, the atomic percentage ratio of Sb:Te in the collected products varies from 41.97%:58.43% to 37.40%:62.60% as the amount of EDTA-Na_2 increases from 1.0 to 4.0 g, respectively. These inorganics, which contain hydroxyl or amino, play a strong role in chelation with Sb^{3+} ions, leading to a decrease of the redox of the Sb^{3+}/Sb pair. Also, the redox of the Sb^{3+}/Sb pair also has an intimate relationship with the addition amount of these inorganics. As a result, the composition of the Sb_2Te_3 products is variable in the presence of different amounts of these inorganics.

3.3. Thermoelectric Properties. To investigate the thermoelectric properties, the Sb_2Te_3 nanobulk materials were made of the powders synthesized at 180 °C without surfactant and with CTAB and PVP, denoted as ST-0, ST-CTAB, and ST-PVP, respectively. The cross-sectional images of the as-annealed Sb_2Te_3 nanobulk materials are shown in Figure 7. From Figure 7a−d, it is clearly seen that the size of the grains in the as-annealed nanobulk materials (ST-0 and ST-CTAB) is much larger than that of their corresponding powders and grains are inclined to grow together. Also, there exist a lot of voids in these

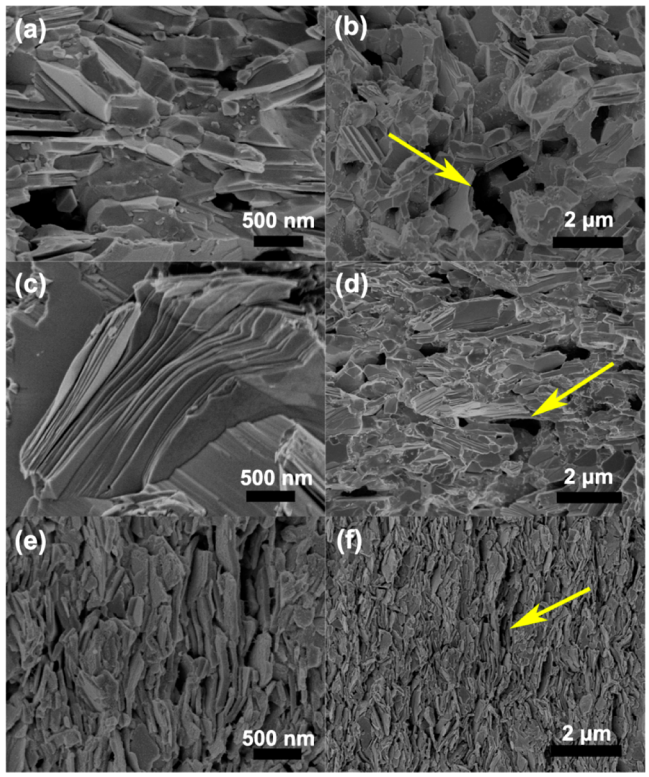

Figure 7. SEM images of the as-annealed Sb_2Te_3 nanobulk materials: (a and b) ST-0; (c and d) ST-CTAB; (e and f) ST-PVP.

DOI: 10.1021/acsami.5b02504
ACS Appl. Mater. Interfaces 2015, 7, 14263−14271

bulk materials, as indicated by the arrows. To be different, the grain growth is not evident in the nanobulk of ST-PVP compared with the size of the corresponding powder, and each of nanoplates is clearly separated because of the PVP residues decorated on the surface of nanoparticles, as shown in Figure 7e,f. It should be noted that lots of voids also present in the ST-PVP nanobulk. As a result, all of these nanobulk materials have a low relative density, ~75% for ST-0, ~81% for ST-CTAB, and ~80% for ST-PVP.

Room temperature Hall measurements were taken on these as-annealed pellets. The results show that the carrier concentration increases from 4.93×10^{19} to 5.00×10^{19} to 5.13×10^{19} cm^{-3}; meanwhile, the hole mobility increases from 93 to 162 to 192 cm^2 V^{-1} s^{-1} for ST-PVP, ST-0, and ST-CTAB, respectively, as given in Table 1. Considering the slight variation in the carrier concentration, the remarkable difference in the hole mobility can be ascribed to variation of the barrier potential of the boundaries. When the grain boundaries are the dominant mechanism of carrier scattering, the mobility can be expressed as follows:[61,62]

Table 1. Relative Density, Hole Concentration *n*, and Hall Mobility μ of the Sb_2Te_3 Nanobulk Materials (ST-0, ST-CTAB, and ST-PVP) at Room Temperature

	relative density (%)	n (10^{19} cm^{-3})	μ (cm^2 V^{-1} S^{-1})
ST-0	74.2	5.00	167
ST-CTAB	81.8	5.13	192
ST-PVP	79.7	4.93	93

$$\mu = (el/\sqrt{8k_BTm^*}) \exp(-E_B/k_BT) \quad (4)$$

where e is the carrier charge, l is the average grain size, k_B is the Boltzmann constant, T is the absolute temperature, m^* is the effective mass of the carrier, and E_B is the potential barrier of the boundaries. From this formula, it can be seen that the lowest mobility in the ST-PVP nanobulk is attributed to the high potential barrier of the boundaries (E_B), which is a result of the existence of PVP residues on the surface of particles. Also, the highest mobility in the ST-CTAB nanobulk is due to the larger grain size and greater density compared with those of the other two samples (ST-PVP and ST-0).

The thermoelectric properties of the as-annealed Sb_2Te_3 nanobulk materials were investigated at temperatures ranging from 40 to 200 °C, and the temperature-dependent resistivity (ρ), Seebeck coefficient (S), power factor (S^2/ρ), and thermal conductivity (κ) are plotted in Figure 8. Figure 8a reveals that the three Sb_2Te_3-nanostructured bulk materials exhibit low electrical resistivity in the range of 10^{-6}–10^{-5} Ω m, which is comparable to that of S-doped Sb_2Te_3 reported by Mehta et al.[19] but much lower than that of other reports on Sb_2Te_3-nanostructured bulk materials.[23,24,34−36] It is worth noting that the low carrier mobility and concentration of the ST-PVP nanobulk lead to its electrical resistivity being ~80% higher than those of the other two nanobulk materials (ST-0 and ST-CTAB). For our three samples, the electrical resistivity increases with the rise of temperature. This increasing trend above room temperature indicates a typical metallic behavior.

The temperature dependence of the Seebeck coefficient of Sb_2Te_3-nanostructured bulk materials is in the range of 103–117 μV K^{-1} at around 47 °C, which is 20–40% higher than that of the corresponding single crystal, 83 μV K^{-1},[63] as shown in Figure 6b. It is generally accepted that the low-energy carriers can lead to a decrease of the Seebeck coefficient and, in turn, their filtering favors enhancement of the Seebeck coefficient. In the case of ST-PVP nanobulk, filtering low-energy carriers by the boundaries with a high barrier potential ensures realization of the highest Seebeck coefficient (117 μV K^{-1} at ~47 °C) and the lowest carrier concentration (4.93×10^{19} cm^{-3} at room temperature) at the same time.

Because each of our Sb_2Te_3-nanostructured materials exhibits a large concentration of free holes, higher than 2.5×10^{19} cm^{-3},[64] all of them can be reasonably regarded as degenerated semiconductors. Therefore, the linear temperature dependence of the Seebeck coefficient can be explained using the semi-classical Mott–Jones formula:[65]

$$S = \frac{8\pi k_B^2}{3eh^2} m^* T \left(\frac{\pi}{3n}\right)^{2/3} \quad (5)$$

where k_B is the Boltzmann constant, h is the Plank constant, m^* is the effective mass of carrier, and e is the charge of the carrier. Additionally, from this equation, we can see that the Seebeck coefficient is inversely proportional to the carrier concentration, $S \sim n^{-2/3}$, which is well demonstrated by the inverse variation trend of the Seebeck coefficient and the hole concentration in our Sb_2Te_3-nanostructured bulk materials.

Naturally, we obtain the high power factor [$(10-16) \times 10^{-4}$ W m^{-1} K^{-2}] in our Sb_2Te_3-nanostructured bulk materials as a result of the relatively low electrical resistivity and the moderate Seebeck coefficient, as shown in Figure 8c. Such high power factor of Sb_2Te_3 nanobulk materials is slightly lower than that of the S-doped Sb_2Te_3-nanostructured bulk material,[19] but much greater than that of other reports on Sb_2Te_3 nanocrystals.[23,24,34−36]

The total thermal conductivity ($\kappa_{tot.}$) is calculated using the formula of $\kappa = D\rho' C_p$, where D is the thermal diffusivity, ρ' is the density, and C_p is the specific heat. It should be noted that the thermal conductivity and electrical resistivity were measured in the orthogonal directions, which are perpendicular to the compaction direction. However, because of the random orientation of the nanoparticles and the strong effect of the boundaries on the electrical and thermal transport properties in the nanostructured materials, the anisotropies of the thermoelectric properties can be significantly reduced.[9] With the strong effect of PVP residues in a ST-PVP nanobulk, the thermal conductivity is significantly decreased from 2.50 W m^{-1} K^{-1} for ST-CTAB to 1.55 W m^{-1} K^{-1} for ST-PVP at 50 °C (Figure 8e). The total thermal conductivity of our annealed Sb_2Te_3 nanobulk materials is strikingly lower than that of the single crystal (5.6 W m^{-1} K^{-1} parallel to the *ab* plane)[63] and the polycrystalline bulk (4.7 W m^{-1} K^{-1} at room temperature)[66] but much larger than that of the other reports on the Sb_2Te_3 nanomaterials (~1 W m^{-1} K^{-1})[19,23,35] mainly because of the long-time annealing. It is believed that the long-time annealing can result in the grain growth and density of the boundary decrease, which, in turn, lead to the thermal conductivity increase. In addition, the thermal diffusivity measurement results also demonstrate that the decrease of the total thermal conductivity of ST-PVP mainly originated from a decrease of the thermal diffusivity compared with that of ST-CTAB; e.g., the thermal diffusivity significantly drops from 1.66×10^{-6} m^2 s^{-1} for ST-CTAB to 1.07×10^{-6} m^2 s^{-1} for ST-PVP at 50 °C, as shown in Figure 8d.

The total thermal conductivity ($\kappa_{tot.}$) usually consists of the electronic thermal conductivity ($\kappa_{el.}$), lattice thermal conductivity ($\kappa_{latt.}$), and bipolar thermal conductivity ($\kappa_{bi.}$); i.e., $\kappa_{tot.} = \kappa_{el.} + \kappa_{latt.} + \kappa_{bi.}$. Considering the monotonic increase of the Seebeck

DOI: 10.1021/acsami.5b02504
ACS Appl. Mater. Interfaces 2015, 7, 14263–14271

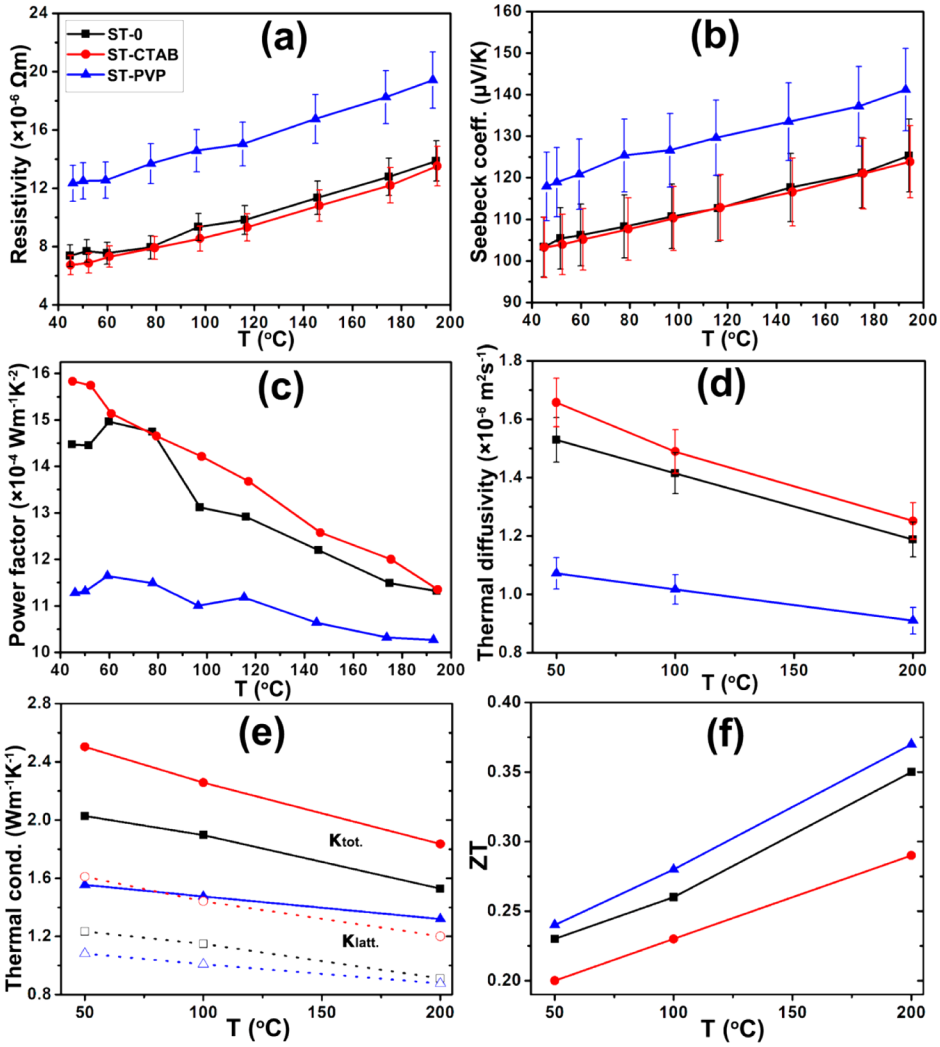

Figure 8. Temperature-dependent thermoelectric properties for different Sb_2Te_3 nanobulk materials (ST-0, ST-CTAB, and ST-PVP): (a) resistivity; (b) Seebeck coefficient; (c) power factor; (d) thermal diffusivity; (e) total thermal conductivity and lattice thermal conductivity; (f) figure of merit, *ZT*. Error bars indicated in parts a, b, and d are plotted on the basis of the measurement uncertainties of resistivity (±10%), Seebeck coefficient (±7%), and thermal diffusivity (±5%), respectively.

coefficient with the temperature, the contribution of bipolar thermal conduction to the total thermal conductivity ($\kappa_{tot.}$) can be ignored. As an alternative, the electronic thermal conductivity ($\kappa_{el.}$) is estimated from the Wiedemann–Franz law, $\kappa_{el.} = LT/\rho$, where L is the Lorentz number. The Lorentz number is calculated using the Fermi integration (see the detailed calculation in the SI). The values of L at 50 °C are obtained as 1.90×10^{-8}, 1.89×10^{-8}, and 1.83×10^{-8} V^2 K^{-2} for ST-CTAB, ST-0, and ST-PVP, respectively. Therefore, the lattice thermal conductivity ($\kappa_{latt.}$) is calculated by subtracting the electronic conduction from the total thermal conductivity ($\kappa_{tot.}$). Owing to the strong phonon scattering by the boundaries in ST-PVP, the lattice thermal conductivity ($\kappa_{latt.}$) decreased from 1.61 W m^{-1} K^{-1} for ST-CTAB to 1.08 W m^{-1} K^{-1} for ST-PVP at 50 °C, as shown in Figure 8e.

Finally, the temperature dependences of *ZT* values for our Sb_2Te_3 nanobulk materials at temperatures of 50–200 °C are displayed in Figure 8f. The ST-PVP sample exhibits the best thermoelectric performance; a maximum value of *ZT* as high as 0.37 is achieved at 200 °C, which is about 25% enhanced by comparison with that of ST-CTAB. The *ZT* value in the range of 0.20–0.37 is comparable to that of other reports on undoped Sb_2Te_3-nanostructured materials[24,36] but much lower than S-doped Sb_2Te_3-nanostructured bulk materials[20] and BiSbTe alloy.[18] It should be noted that the relatively low *ZT* of our Sb_2Te_3 nanobulk materials is mainly due to the high thermal conductivity, nearly doubled in comparison with that of other Sb_2Te_3-nanostructured materials. It is believed that the long-time annealing after cold pressing is the main reason leading to the high thermal conductivity of our Sb_2Te_3-nanostructured materials. The advanced molding technologies, i.e., spark plasma sintering, will be tested for further enhancement of the thermoelectric performance of our Sb_2Te_3-nanostructured materials in future work.

4. CONCLUSIONS

In summary, we synthesized the good crystalline Sb_2Te_3 nanoplates for thermoelectric application via a simple, low-cost, and scalable reflux method in the solvent EG in the low-temperature range of 120–180 °C. Also, the formation mechanism of platelike morphology was proposed, and the effect of organic surfactants or inorganic salts (CTAB, PVP, EDTA-Na_2, NaOH, etc.) on the size, morphology, and purity of the resultant Sb_2Te_3 product was investigated. Subsequently,

DOI: 10.1021/acsami.5b02504
ACS Appl. Mater. Interfaces 2015, 7, 14263–14271

Sb_2Te_3-nanostructured bulk materials were fabricated via cold compaction followed by the annealing process for investigation of the thermoelectric properties. The results show that our Sb_2Te_3 nanobulk materials exhibit low resistivity [$(7.37-19.4) \times 10^{-6}$ Ω m], moderate Seebeck coefficients (103−141 μV K^{-1}), and high power factors [$(10-16) \times 10^{-4}$ W m^{-1} K^{-2}]. Furthermore, the highest *ZT* value of 0.37 is obtained in the ST-PVP sample at 200 °C. On the basis of this work, it is worth noting that some organic residue coating on the surface of the particles could tune the barrier potential of the boundaries and, in turn, remarkably vary the electrical and thermal transport properties of the nanostructured materials; as an alternative, some inorganic salts that contain hydroxyl or amino can play a role in chelating with metal ions, making the composition of the products controllable. Our research provides a simple and economic surfactant-assisted reflux method to fabricate Sb_2Te_3 nanoplates with enhanced thermoelectric properties for the applications of low-temperature waste heat recovery or cooling devices.

■ ASSOCIATED CONTENT

Supporting Information

FTIR spectra of the as-prepared Sb_2Te_3 nanoparticles without or with surfactant (CTAB, PVP) and pure CTAB and PVP, XRD patterns and EDS results for the Sb_2Te_3 products in the presence of EDTA-Na_2 and NaOH, and details of the Lorenz number calculation. The Supporting Information is available free of charge on the ACS Publications website at DOI: 10.1021/acsami.5b02504.

■ AUTHOR INFORMATION

Corresponding Author

*E-mail: miaolei@ms.giec.ac.cn.

Notes

The authors declare no competing financial interest.

■ ACKNOWLEDGMENTS

This work was supported by the National Natural Science Foundation of China (Grant 51172234), Science and Technology Planning Project of Guangdong Province, China (Grant 2013B050800006), and External Cooperation Program of BIC, Chinese Academy of Sciences (Grant 182344KYSB20130006).

■ REFERENCES

(1) Ioffe, A. F. *Semiconductor Thermoelements and Thermoelectric Cooling*; Infosearch: London, 1957; pp 3−8.
(2) DiSalvo, F. J. Thermoelectric Cooling and Power Generation. *Science* **1999**, *285*, 703−706.
(3) Bell, L. E. Cooling, Heating, Generating Power, and Recovering Waste Heat with Thermoelectric Systems. *Science* **2008**, *321*, 1457−1461.
(4) Tritt, T. M.; Subramanian, M. A. Thermoelectric Materials, Phenomena, and Applications: A Bird's Eye View. *MRS Bull.* **2006**, *31*, 188−198.
(5) Minnich, A. J.; Dresselhaus, M. S.; Ren, Z. F.; Chen, G. Bulk Nanostructured Thermoelectric Materials: Current Research and Future Prospects. *Energy Environ. Sci.* **2009**, *2*, 466−479.
(6) Lan, Y. C.; Minnich, A. J.; Chen, G.; Ren, Z. F. Enhancement of Thermoelectric Figure-of-Merit by a Bulk Nanostructuring Approach. *Adv. Funct. Mater.* **2010**, *20*, 357−376.
(7) Sootsman, J. R.; Chung, D. Y.; Kanatzidis, M. G. New and Old Concepts in Thermoelectric Materials. *Angew. Chem., Int. Ed.* **2009**, *48*, 8616−8639.
(8) Kim, S. I.; Lee, K. H.; Mun, H. A.; Kim, H. S.; Hwang, S. W.; Roh, J. W.; Yang, D. J.; Shin, W. H.; Li, X. S.; Lee, Y. H.; Snyder, G. J.; Kim, S. W. Dense Dislocation Arrays Embedded in Grain Boundaries for High-Performance Bulk Thermoelectrics. *Science* **2015**, *348*, 109−114.
(9) Poudel, B.; Hao, Q.; Ma, Y.; Lan, Y. C.; Minnich, J. A.; Yu, B.; Yan, X.; Wang, D. Z.; Muto, A.; Vashaee, D.; Chen, X. Y.; Liu, J. M.; Dresselhaus, M. S.; Chen, G.; Ren, Z. F. High-Thermoelectric Performance of Nanostructured Bismuth Antimony Telluride Bulk Alloys. *Science* **2008**, *320*, 634−638.
(10) Xie, W. J.; He, J.; Kang, H. J.; Tang, X. F.; Zhu, S.; Laver, M.; Wang, S. Y.; Copley, J. R. D.; Brown, C. M.; Zhang, Q. J.; Tritt, T. M. Identifying the Specific Nanostructures Responsible for the High Thermoelectric Performance of $(Bi,Sb)_2Te_3$ Nanocomposites. *Nano Lett.* **2010**, *10*, 3283−3289.
(11) Biswas, K.; He, J. Q.; Blum, I. D.; Wu, C. I.; Hogan, T. P.; Seidman, D. N.; Dravid, V. P.; Kanatzidis, M. G. High-performance Bulk Thermoelectrics with All-Scale Hierarchical Architectures. *Nature* **2012**, *489*, 414−418.
(12) Wu, H. J.; Zhao, L. D.; Zheng, F. S.; Wu, D.; Pei, Y. L.; Tong, X.; Kanatzidis, M. G.; He, J. Q. Broad Temperature Plateau for Thermoelectric Figure of Merit *ZT* > 2 in Phase-Separated $PbTe_{0.7}S_{0.3}$. *Nat. Commun.* **2014**, *5*, 4515.
(13) Goldsmid, H. J. Recent Studies of Bismuth Telluride and Its Alloys. *J. Appl. Phys.* **1961**, *32*, 2198−2202.
(14) Yavorsky, B. Y.; Hinsche, N. F.; Mertig, I.; Zahn, P. Electronic Structure and Transport Anisotropy of Bi_2Te_3 and Sb_2Te_3. *Phys. Rev. B* **2011**, *84*, 165208.
(15) Horák, J.; Starý, Z.; Klikorka, J. Relations between Structure, Bonding, and Nature of Point Defects in Layered Crystals of Tetradymite Structure. *Phys. Status Solidi B* **1988**, *147*, 501−510.
(16) Horák, J.; Drašar, Č.; Novotný, R.; Karamazov, S.; Lošťák, P. Non-Stoichiometry of the Crystal Lattice of Antimony Telluride. *Phys. Status Solidi A* **1995**, *149*, 549−556.
(17) Drašar, Č.; Steinhart, M.; Lošťák, P.; Shin, H. K.; Dyck, J. S.; Uher, C. Transport Coefficients of Titanium-Doped Sb_2Te_3 Single Crystals. *J. Solid State Chem.* **2005**, *178*, 1301−1307.
(18) Drašar, Č.; Lošťák, P.; Uher, C. Doping and Defect Structure of Tetradymite-Type Crystals. *J. Electron. Mater.* **2010**, *39*, 2162−2164.
(19) Mehta, R. J.; Zhang, Y. L.; Zhu, H.; Parker, D. S.; Belley, M.; Singh, D. J.; Ramprasad, R.; Borca-Tasciuc, T.; Ramanath, G. Seebeck and Figure of Merit Enhancement in Nanostructured Antimony Telluride by Antisite Defect Suppression through Sulfur Doping. *Nano Lett.* **2012**, *12*, 4523−4529.
(20) Lošťák, P.; Horák, J. Optical and Transport Properties of the $Sb_{2-x}In_xTe_3$ Single Crystals. *Phys. Scr.* **1988**, *37*, 812−815.
(21) Dhar, S. N.; Desai, C. F. Sb_2Te_3 and $In_{0.2}Sb_{1.8}Te_3$: A comparative study of thermoelectric and related properties. *Philos. Mag. Lett.* **2002**, *82*, 581−587.
(22) Zhou, B.; Ji, Y.; Yang, Y. F.; Li, X. H.; Zhu, J. J. Rapid Microwave-Assisted Synthesis of Single-Crystalline Sb_2Te_3 Hexagonal Nanoplates. *Cryst. Growth Des.* **2008**, *8*, 4394−4397.
(23) Dong, G. H.; Zhu, Y. J.; Chen, L. D. Microwave-Assisted Rapid Synthesis of Sb_2Te_3 Nanosheets and Thermoelectric Properties of Bulk Samples Prepared by Spark Plasma Sintering. *J. Mater. Chem.* **2010**, *20*, 1976−1981.
(24) Dong, G. H.; Zhu, Y. J.; Chen, L. D. Sb_2Te_3 Nanostructures with Various Morphologies: Rapid Microwave Solvothermal Synthesis and Seebeck Coefficients. *CrystEngComm* **2011**, *13*, 6811−6816.
(25) Mehta, R. J.; Zhang, Y. L.; Karthik, C.; Singh, B.; Siegel, R. W.; Borca-Tasciuc, T.; Ramanath, G. A New Class of Doped Nanobulk High-Figure-of-Merit Thermoelectrics by Scalable Bottom-Up Assembly. *Nat. Mater.* **2012**, *11*, 233−240.
(26) Wang, W. Z.; Poudel, B.; Yang, J.; Wang, D. Z.; Ren, Z. F. High-Yield Synthesis of Single-Crystalline Antimony Telluride Hexagonal Nanoplates Using a Solvothermal Approach. *J. Am. Chem. Soc.* **2005**, *127*, 13792−13793.
(27) Shi, W. D.; Yu, J. B.; Wang, H. S.; Zhang, H. J. Hydrothermal Synthesis of Single-Crystalline Antimony Telluride Nanobelts. *J. Am. Chem. Soc.* **2006**, *128*, 16490−16491.

DOI: 10.1021/acsami.5b02504
ACS Appl. Mater. Interfaces 2015, 7, 14263−14271

(28) Shi, W. D.; Zhou, L.; Song, S. Y.; Yang, J. H.; Zhang, H. J. Hydrothermal Synthesis and Thermoelectric Transport Properties of Impurity-Free Antimony Telluride Hexagonal Nanoplates. *Adv. Mater.* **2008**, *20*, 1892−1897.
(29) Shi, S. F.; Cao, M. H.; Hu, C. W. Controlled Solvothermal Synthesis and Structural Characterization of Antimony Telluride Nanoforks. *Cryst. Growth Des.* **2009**, *9*, 2057−2060.
(30) Zhang, G. Q.; Wang, W.; Lu, X. L.; Li, X. G. Solvothermal Synthesis of V−VI Binary and Ternary Hexagonal Platelets: The Oriented Attachment Mechanism. *Cryst. Growth Des.* **2009**, *9*, 145−150.
(31) Yuan, Q. L.; Nie, Q. L.; Huo, D. X. Preparation and Characterization of the Antimony Telluride Hexagonal Nanoplates. *Curr. Appl. Phys.* **2009**, *9*, 224−226.
(32) Datta, A.; Paul, J.; Kar, A.; Patra, A.; Sun, Z. L.; Chen, L. D.; Martin, J.; Nolas, G. S. Facile Chemical Synthesis of Nanocrystalline Thermoelectric Alloys Based on Bi−Sb−Te−Se. *Cryst. Growth Des.* **2010**, *10*, 3983−3989.
(33) Wang, W. Z.; Long, D.; Liang, Y. J.; Zhang, G. L.; Zeng, B. Q.; He, Q. Y. Conversion of Hexagonal Sb_2Te_3 Nanoplates into Nanorings Driven by Growth Temperature. *Langmuir* **2011**, *27*, 815−819.
(34) Jin, R. C.; Chen, G.; Pei, J.; Xu, H. M.; Lv, Z. S. Solvothermal Synthesis and Growth Mechanism of Ultrathin Sb_2Te_3 Hexagonal Nanoplates with Thermoelectric Transport Properties. *RSC Adv.* **2012**, *2*, 1450−1456.
(35) Sun, S. L.; Peng, J.; Jin, R. X.; Song, S. Y.; Zhu, P. W.; Xing, Y. Template-Free Solvothermal Synthesis and Enhanced Thermoelectric Performance of Sb_2Te_3 Nanosheets. *J. Alloys Compd.* **2013**, *558*, 6−10.
(36) Dong, G. H.; Zhu, Y. J.; Cheng, G. F.; Ruan, Y. J. Sb_2Te_3 Nanobelts and Nanosheets: Hydrothermal Synthesis, Morphology Evolution and Thermoelectric Properties. *J. Alloys Compd.* **2013**, *550*, 164−168.
(37) Zhou, N.; Chen, G.; Zhang, X. S.; Xu, Y. C.; Xu, B. R.; Li, M. Q. Size-Controlled Synthesis and Transport Properties of Sb_2Te_3 Nanoplates. *RSC Adv.* **2014**, *4*, 2427−2432.
(38) Christian, P.; O'Brien, P. The Preparation of Antimony Chalcogenide and Oxide Nanomaterials. *J. Mater. Chem.* **2005**, *15*, 4949−4954.
(39) Srivastava, P.; Singh, K. Layered Sb_2Te_3 Nanoflakes as Chalcogenide Dielectrics. *J. Electron. Mater.* **2013**, *42*, 2733−2738.
(40) Yang, H. Q.; Miao, L.; Zhang, M.; Ohno, K.; Zhou, J. H.; Gu, H.; Shen, Y.; Lin, H. Low-Temperature, Solution-Based, Scalable Synthesis of Sb_2Te_3 Nanoparticles with an Enhanced Power Factor. *J. Electron. Mater.* **2014**, *43*, 2165−2173.
(41) Jin, C. G.; Zhang, G. Q.; Qian, T.; Li, X. G.; Yao, Z. Large-Area Sb_2Te_3 Nanowire Arrays. *J. Phys. Chem. B* **2005**, *109*, 1430−1432.
(42) Pinisetty, D.; Gupta, M.; Karki, A. B.; Young, D. P.; Devireddy, R. V. Fabrication and Characterization of Electrodeposited Antimony Telluride Crystalline Nanowires and Nanotubes. *J. Mater. Chem.* **2011**, *21*, 4098−4107.
(43) Schumacher, C.; Reinsberg, K. G.; Akinsinde, L.; Zastrow, S.; Heiderich, S.; Toellner, W.; Rampelberg, G.; Detavernier, C.; Broekaert, J. A. C.; Nielsch, K.; Bachmann, J. Optimization of Electrodeposited p-Doped Sb_2Te_3 Thermoelectric Films by Millisecond Potentiostatic Pulses. *Adv. Energy Mater.* **2012**, *2*, 345−352.
(44) Garje, S. S.; Eisler, D. J.; Ritch, J. S.; Afzaal, M.; O'Brien, P.; Chivers, T. A New Route to Antimony Telluride Nanoplates from a Single-Source Precursor. *J. Am. Chem. Soc.* **2006**, *128*, 3120−3121.
(45) Knapas, K.; Hatanpää, T.; Ritala, M.; Leskelä, M. In Situ Reaction Mechanism Studies on Atomic Layer Deposition of Sb_2Te_3 and GeTe from $(Et_3Si)_2Te$ and Chlorides. *Chem. Mater.* **2010**, *22*, 1386−1391.
(46) Schulz, S.; Heimann, S.; Friedrich, J.; Engenhorst, M.; Schierning, G.; Assenmacher, W. Synthesis of Hexagonal Sb_2Te_3 Nanoplates by Thermal Decomposition of the Single-Source Precursor $(Et_2Sb)_2Te$. *Chem. Mater.* **2012**, *24*, 2228−2234.
(47) Meister, S.; Peng, H. L.; McIlwrath, K.; Jarausch, K.; Zhang, X. F.; Cui, Y. Synthesis and Characterization of Phase-Change Nanowires. *Nano Lett.* **2006**, *6*, 1514−1517.
(48) Lee, J. S.; Brittman, S.; Yu, D.; Park, H. Vapor−Liquid−Solid and Vapor−Solid Growth of Phase-Change Sb_2Te_3 Nanowires and Sb_2Te_3/GeTe Nanowire Heterostructures. *J. Am. Chem. Soc.* **2008**, *130*, 6252−6258.
(49) Chen, J.; Sun, T.; Sim, D. H.; Peng, H. Y.; Wang, H. T.; Fan, S. F.; Hng, H. H.; Ma, J.; Boey, F. Y. C.; Li, S.; Samani, M. K.; Chen, G. C. K.; Chen, X. D.; Wu, T.; Yan, Q. Y. Sb_2Te_3 Nanoparticles with Enhanced Seebeck Coefficient and Low Thermal Conductivity. *Chem. Mater.* **2010**, *22*, 3086−3092.
(50) Duan, X. K.; Jiang, Y. Z. Synthesis of Sb_2Te_3 Nanopowders by Vacuum Arc Plasma Evaporation. *Vacuum* **2011**, *85*, 1052−1054.
(51) Kahlwext, M. Ostwald Ripening of Precipitates. *Adv. Colloid Interface Sci.* **1975**, *5*, 1−35.
(52) Yin, Y. D.; Alivisatos, A. P. Colloidal nanocrystal synthesis and the organic−inorganic interface. *Nature* **2004**, *437*, 664−670.
(53) Zhang, G. Q.; Kirk, B.; Jauregui, L. A.; Yang, H.; Xu, X. F.; Chen, Y. P.; Wu, Y. Rational Synthesis of Ultrathin n-Type Bi_2Te_3 Nanowires with Enhanced Thermoelectric Properties. *Nano Lett.* **2012**, *12*, 56−60.
(54) Son, J. S.; Choi, M. K.; Han, M. K.; Park, K.; Kim, J. Y.; Lim, S. J.; Oh, M.; Kuk, Y.; Park, C.; Kim, S. J.; Hyeon, T. n-Type Nanostructured Thermoelectric Materials Prepared from Chemically Synthesized Ultrathin Bi_2Te_3 Nanoplates. *Nano Lett.* **2012**, *12*, 640−647.
(55) Tai, G. A.; Zhou, B.; Guo, W. L. Structural Characterization and Thermoelectric Transport Properties of Uniform Single-Crystalline Lead Telluride Nanowires. *J. Phys. Chem. C* **2008**, *112*, 11314−11318.
(56) Liang, H. W.; Liu, S.; Wu, Q. S.; Yu, S. H. An Efficient Templating Approach for Synthesis of Highly Uniform CdTe and PbTe Nanowires. *Inorg. Chem.* **2009**, *48*, 4927−4933.
(57) Yang, H. R.; Bahk, J. H.; Day, T.; Mohammed, A. M. S.; Min, B.; Snyder, G. J.; Shakouri, A.; Wu, Y. Composition Modulation of Ag_2Te Nanowires for Tunable Electrical and Thermal Properties. *Nano Lett.* **2014**, *14*, 5398−5404.
(58) Xia, Y. N.; Xiong, Y. J.; Lim, B.; Skrabalak, S. E. Shape-Controlled Synthesis of Metal Nanocrystals:Simple Chemistry Meets Complex Physics? *Angew. Chem., Int. Ed.* **2009**, *48*, 60−103.
(59) Zhuang, Z. B.; Peng, Q.; Li, Y. D. Controlled Synthesis of Semiconductor Nanostructures in the Liquid Phase. *Chem. Soc. Rev.* **2011**, *40*, 5492−5513.
(60) Gao, M. R.; Xu, Y. F.; Jiang, J.; Yu, S. H. Nanostructured Metal Chalcogenides: Synthesis, Modification, and Applications in Energy Conversion and Storage Devices. *Chem. Soc. Rev.* **2013**, *42*, 2986−3017.
(61) Seto, J. Y. W. The Electrical Properties of Polycrystalline Silicon Films. *J. Appl. Phys.* **1975**, *46*, 5247.
(62) Martin, J.; Wang, L.; Chen, L. D.; Nolas, G. S. Enhanced Seebeck Coefficient Through Energy-Barrier Scattering in PbTe Nanocomposites. *Phys. Rev. B* **2009**, *79*, 115311.
(63) Rowe, D. M. *Thermoelectrics Handbook: Macro to Nano*; CRC Press: New York, 2006; section III, Chapter 27, p 16.
(64) Ioffe, A. F. *Semiconductor Thermoelements and Thermoelectric Cooling*; Infosearch: London, 1957; p 45.
(65) Cutler, M.; Leavy, J. F.; Fitzpatrick, R. L. Electronic Transport in Semimetallic Cerium Sulfid. *Phys. Rev.* **1964**, *133*, A1143.
(66) Touloukian, Y. S.; DeWitt, D. P. *Thermal Conductivity: Metallic Elements and Alloys*; IFI/Plenum: New York, 1970.

NOTE ADDED AFTER ASAP PUBLICATION

This paper was published on the Web on June 23, 2015, with minor text corrections. The corrected version was reposted on June 25, 2015.

DOI: 10.1021/acsami.5b02504
ACS Appl. Mater. Interfaces 2015, 7, 14263−14271